# Discontinuous plastic flow in stainless steels subjected to combined loads at extremely low temperatures

J. Tabin [a,b,*], B. Skoczeń [a], J Bielski [a]

[a] Institute of Applied Mechanics, Faculty of Mechanical Engineering, Cracow University of Technology, 31-864 Cracow, Poland
[b] Institute of Fundamental Technological Research, Polish Academy of Sciences, 02-106 Warsaw, Poland

## ARTICLE INFO

## ABSTRACT

In the present paper, the question of the mechanism of discontinuous plastic flow (DPF) occurring at extremely low temperatures (in the proximity of absolute zero), is for the first time raised in the context of kinematically controlled combined loads (independent control of displacement and rotation) and non-proportional loading paths. In order to identify the multiaxial stress state during DPF, a unique set-up for testing tubular samples under kinematically controlled traction and torsion in liquid helium (4.2 K) has been developed. The results of tests performed on grade 304 stainless steel thin-walled tubular samples subjected to combined loads (traction and torsion) in the proximity of absolute zero are for the first time reported. These novel results confirm the assumptions accepted when building the multiaxial constitutive model of discontinuous plastic flow, namely, the production of lattice barriers, the pile-ups of dislocations and the criterion of their collective failure, as well as the assumption that the serrations may be recorded by force and torque transducers independently. Thus, the numerically implemented model allows to reproduce the observed serrations, and to redistribute them between the loading directions.

## 1. Introduction

Modern science needs very sophisticated and complex instruments in order to explore the micro and the macro cosmos. The basic constituents of matter are intensively investigated by the Large Hadron Collider (CERN, Geneva), while large objects such as Mars by NASA's Perseverance rover. In order to perform such a demanding exploration, all equipment components were initially tested at cryogenic temperatures. The main magnets of the LHC operate in superfluid helium at the temperature of 1.9 K, while the temperatures near the Mars poles can drop down to 148 K.

There is a large variety of materials suitable for application at extremely low temperatures, such as the austenitic stainless steels (304, 316LN, etc.), the copper alloys (C1500, Cu OFE), the high-entropy alloys (CrMnFeCoNi, Al0.5CoCrCuFeNi) or the composite materials (Cu-NbTi, Cu-Nb3Sn, etc.).

Fcc metals and alloys (e.g. austenitic stainless steels, copper alloys or selected composite materials) are applied in superconducting magnets or cryogenic transfer and storage systems within the whole range of temperatures, from near-0 K to ambient temperature. They show high ductility at extremely low temperatures [11,25,27,40]. For example, austenitic stainless steel was chosen for load-bearing structures of large superconducting magnets [8,57] in the LHC (CERN), whereas the super-

conducting composite materials (Cu-Nb$_3$Sn) were selected for the coils in five-coil damping wigglers [9], currently tested in High Luminosity LHC. Moreover, superconducting wires and tapes based on the copper alloys are commonly used in high power applications including power cables, motors, generators and solenoid high field magnets [7].

Recently, high-entropy alloys (HEAs) become more popular [49]. Except of high ductility, they exhibit at cryogenic temperatures high hardness, oxidation resistance, corrosion resistance, resistance to temperature softening, wear resistance, fatigue, and fracture resistance [12]. Tsai and Yeh. [49] identified that the stacking fault energy (SFE) of CoCrFeMnNi is close to conventional low-SFE alloys, such as the austenitic stainless steels (e.g. 304L) and brass. These remarkable properties make HEAs suitable advanced structural materials for many low temperature industries, including aerospace and ocean engineering [13]. Nevertheless, HEA's manufacturing process is much more complicated and expensive than for the austenitic stainless steels, therefore the latter ones are still commonly used at cryogenic temperatures [15].

The behaviour of the above discussed materials at extremely low temperatures is radically different than at room or enhanced temperatures. In particular, when straining the samples in liquid helium (4.2 K), the oscillatory mode of plastic flow is observed [25,30,31,45,48]. This mode is reflected by sudden drops of stress against strain (or time, Fig. 1), accompanied by Dirac-like temperature spikes (blue curve) coupled to the drops of stress (Fig. 4b). It is worth pointing out that the appearance of discontinuous plastic flow (DPF) is quite similar to the appearance of the so-called Portevin – Le Chatelier effect (PLC)
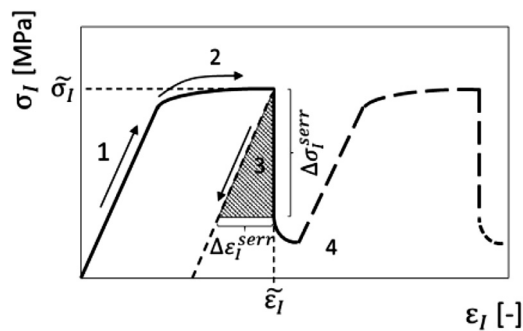
**Fig. 1.** Single serration in direction I for stress-strain curve: (1) elastic loading, (2) smooth plastic flow, (3) drop of stress and macroscopic slip, (4) relaxation.

[16,19,22,29], i.e. the abrupt stress oscillations as a function of time or strain occurring during a displacement controlled traction test. The difference between both mechanisms consists in the fact that in the case of PLC the obstacles are created by diffusion, whereas, in the case of DPF the obstacles are diffusionless [31]. Unlike the Portevin - Le Chatelier effect based on diffusion and motion of dislocations in the selected metals, the low temperature discontinuous plastic flow is essentially a universal effect occurring in almost all materials at the temperatures below some critical limit [25,51]: from pure metals, such as Al, Nb, Re, Mo and W [3,4,20], through austenitic stainless steels [24–26,39,45] to the glass fibre-epoxy composites [17,32,47] or fcc-based high entropy alloy [30,49]. Despite extensive efforts to investigate the DPF [31], there has been no explanation yet of this discrepancy due to the complicated nature of the plastic flow instabilities [30].

Therefore, in order to explain this effect, extensive studies were conducted, including the kinematically controlled tests at extremely low temperatures (the notion "kinematically controlled" refers to displacement control). However, a real breakthrough came with the development of special set-up for testing tubular samples under combined loads, comprising axial tension (stretch) and torsion. Such a combination of loads, rather unique at extremely low temperatures, has one great advantage – fast development of shear strains causing practically immediate plastic flow of the sample. Moreover, in the tubular sample subjected to tension and torsion all its sections are simultaneously deformed and enter the yielding regime at the same time. This is crucial for correct understanding of the mechanisms that accompany the plastic flow of ductile materials at very low temperatures. A sequence of tests under combined kinematically controlled loads led to much better understanding of the so called multiaxial discontinuous plastic flow (MDPF). In the uniaxial tests, axial displacement was controlled by the constant crosshead movement. In the biaxial tests, axial displacement was controlled as above, whereas the angular displacement was controlled by the imposed constant angular velocity.

Discontinuous plastic flow, often termed serrated yielding or intermittent plastic flow, has been studied in the past mostly experimentally. Some initial work on this particular phenomenon was carried out by [2]. Later on, a contribution to better understanding of serrated yielding was added by [14,33,34,37,56], or [31], who collected and systematized the experimental data, and recalled the main characteristics of the plastic flow instabilities at cryogenic temperatures. In the context of complex loadings at cryogenic temperatures, the overview should be supplemented by important contributions by Zinov'ev et al. [59] and Vorob'ev [52].

[2], was the first to attribute the load drops to the thermodynamic properties of the materials at very low temperatures. In particular, he developed the adiabatic heating hypothesis, based on the assumption that during a sufficiently fast dissipative process at very low temperatures, an increase of temperature and a consequent decrease of the flow stress is observed. This leads to negative slope of the flow stress against

temperature, and possible consequence in the form of drop of stress. However, starting from the same years, other authors like [54], or [43], developed a different approach stating that high flow stresses at very low temperatures induce avalanche-like production of mobile dislocations that may be at the origin of observed serrations.

Yet, another explanation of serrated yielding was proposed by [56], who attributed the plastic flow discontinuities at extremely low temperatures to the well-known strain rate softening instabilities. Moreover, the Authors pointed out a number of similar features between the DPF and the PLC, characteristic for room temperature and specific materials like iron. As the strain rate sensitivity consists in the instantaneous and positive response of the flow stress to sudden increase of the strain rate, the response of materials during DPF seems to follow this pattern. Especially, that the primary response is followed by a relaxation of stress to asymptotic value, which is also observed in some materials at extremely low temperatures. Theoretical and numerical modelling of the PLC instabilities from the physical and the phenomenological point of view was presented by Rizzi and Hähner [36].

An interesting analysis, leading to better understanding of the mechanism of DPF, can be found in Vorob'ev [50] and Vorob'ev and Anpilogova [51,53]. The objective of these papers is to systematize and classify the limit states and to obtain the criteria of DPF. The Authors determined main factors that influence the plastic flow instability at cryogenic temperatures, namely: the loading conditions, the strain rate, the thermal and the physical characteristics of the cooling medium, the rigidity of the loading system and the loading regime, as well as the presence of initial strains and stress concentrations, the size and the shape of the deformed object, etc. [53]. Based on the experimental results and the analysis of materials, the recommendations were formulated on how to improve tensile testing of materials at cryogenic temperatures, especially in liquid helium (LHe). Moreover, a numerical analysis of discontinuous plastic flow of metals, including the above-mentioned factors and using the thermomechanical model [50], was proposed. It has been shown that most of the potential strain energy is converted to work.

It turns out, however, that the problem is even more complicated, which was clearly shown in the works by [25,26]. The Authors, in their attempt to explain DPF, made reference to the work by [38]. They assumed namely, that the pile-ups of dislocations form on the internal barriers in the weakly excited lattice and induce such stress concentrations, that may reach the level of the shear strength. Moreover, they assumed that a catastrophic process of breaking down the lattice barriers takes place, leading to macroscopic slip and abrupt drop of stress. This process may be followed by further generation of dislocations, as soon as the internal barriers are broken.

In the context of thermomechanical approach, a model of DPF has been developed by Estrin and Kubin [10]. The heat conduction equations and the mechanical description were adopted in the derivation of the plastic flow instability criterion. Later on, a physically-based, multiscale model of DPF has been developed by [39], and [40,41], where both effects were included: accumulation of dislocations and failure of lattice barriers, as well as the adiabatic heating, leading to substantial temperature rise. The main feature of this model consists in the fact, that the plastic power released in the course of drop of stress and converted to heat is the main cause of temperature rise, which finally contributes to stress relaxation. This uniaxial model proved its validity during numerous cross-checks with the experimental results, obtained by means of the in-house set-up [40,41,44–48]. In particular, the correct sequence of events during single serration, including: elastic loading, smooth plastic flow, drop of stress accompanied by temperature spike, and stress relaxation (Fig. 1) has been confirmed. Natural consequence of development of the model consists in raising the question, whether the discontinuous plastic flow is observed under the multiaxial state of stress, and if the model can possibly by stretched over combined loads and non-proportional loading paths. To this end, unique set-up for testing tubular samples under combined loads (tension and torsion) has been built and calibrated at the temperature of liquid helium. Moreover, the

constitutive model of DPF was extended to the multiaxial stress state, including the normal and the shear stresses. Finally, the numerical simulations were performed in order to cross-check the results with the experimental data. To the knowledge of the authors, the present paper is the first consistent attempt to explain the plastic flow discontinuities at extremely low temperatures in the context of combined loads and non-proportional loading paths. Here, non-proportional loads (non-proportional loading paths) refer to such a loading scheme, where both loading components change in an independent way (are not proportional to a common factor). It means that the loading program has to be defined for each loading component separately. On the other hand, the proportional loads (proportional loading paths) reflect the situation when both loading components increase proportionally to a common factor (control parameter).

An interesting approach to non-proportional cyclic plasticity has been recently presented by H. Wu [55], who indicated that the non-proportional hardening may affect the fatigue life of materials subjected to multiaxial low-cycle fatigue loading. The Author indicated that such microstructural phenomena, like the increase of stacking faults, formation of micro-twins or nucleation of martensite particles, can introduce - for non-proportional loading - significant strain hardening effect. Also, new micro-plane model has been developed by T. Zhou at al. [58] in order to predict the non-proportional, multiaxial deformation of shape memory alloys, including the martensite transformation and the reorientation. Recently, F. Barlat et al. [1] have developed a substantially modified version of the well-known homogeneous anisotropic hardening (HAH) framework. In particular, an improved distortional plasticity model, describing the anisotropic hardening that occurs during the strain path changes (e.g. the Bauschinger and the cross-loading effects), has been demonstrated and applied.

The main goal of the present paper consists in identification of DPF in the context of kinematically controlled combined loads. Based on the experimental results, the DPF phenomenon is thoroughly explained and the mathematical description of DPF (uniaxial and multiaxial) is presented. In order to verify the basic assumptions of the model, a campaign of tests was carried out to investigate simple tension and combined loads. The general multiaxial model was then reduced to biaxial case of tension and torsion. Finally, the results of numerical simulations were compared with the experimental data and good convergence was achieved.

## 2. Modelling of multiaxial DPF

Modelling of DPF for applications at extremely low temperatures requires an insight into the phenomena that occur in the proximity of absolute zero, including the so-called thermodynamic instability. The instability results from the 3$^{rd}$ principle of thermodynamics for perfect crystals, which states that the entropy tends to zero with temperature. This consequently implies similar behaviour of such thermodynamic quantities like the specific heat, the thermal conductivity and the thermal expansion coefficient. Also, the DPF model is based on the assumption that all the mathematically described processes are embedded in the mesoscopic representative volume element (RVE), and their characteristic wave length is small when compared to the size of the RVE. The main components of the model, including the kinetics of the DPF, are first formulated in the RVE, and then generalized to the macroscopic scale.

### 2.1. Thermodynamic background

DPF is a dissipative process during which heat generation occurs. The heat transport in the lattice is essentially represented by two mechanisms: the phonons and the free electrons. Moreover, the quantum lattice vibrations (phonons) are limited to the acoustic modes only. The overall energy of the quantum lattice vibrations is computed by means

of the Debye theory (assuming linear dispersion law):

$$E_{ph} \sim NT^4/\Theta^3 \qquad (1)$$

where $N$ is the number of atoms (cells) in the lattice, $T$ is the temperature, and $\theta$ is the normalized reference temperature. The specific heat under constant volume is obtained by means of differentiation of the above term with respect to temperature:

$$\left(C_{ph}\right)_V = \partial_T E_{ph}|_V \sim NT^3/\Theta^3 \qquad (2)$$

The contribution of free electrons to the specific heat is expressed by:

$$\left(C_{el}\right)_V \sim T/T_F \qquad (3)$$

where $T_F$ denotes the Fermi reference temperature. Finally, the specific heat reads:

$$C_V = \left(C_{el}\right)_V + \left(C_{ph}\right)_V \sim T/T_F + NT^3/\Theta^3 \qquad (4)$$

As the heat increment is related to temperature increment by the following equation:

$$dQ = mC_V dT \Rightarrow dT/dQ = \left(mC_V\right)^{-1} \qquad (5)$$

one obtains:

$$T \to 0, \; C_V \to 0 \Rightarrow dT/dQ \to \infty \qquad (6)$$

Thus, any increment of energy deposited in the lattice at extremely low temperatures (for instance due to plastic power dissipation), will produce – under the adiabatic conditions – a substantial temperature rise. The phenomenon of thermodynamic instability has been so far expressed in terms and by means of pure thermodynamic functions. Thermodynamic instability plays an important role in the explanation of discontinuous plastic flow, since it elucidates the increase of temperature in the form of temperature spike (Fig. 4) just after the macroscopic slip, that results from collapse of local lattice barriers under the stresses caused by the pile-ups of dislocations. It may clearly take the form of thermomechanical instability that occurs when the mechanical effect becomes the source of heat. For instance, a macroscopic slip in the lattice may contribute to heat dissipation and - under nearly adiabatic conditions – may cause increase of temperature in the form of temperature spike. The origin, however, is fully thermodynamic and results from the third principle of thermodynamics.

### 2.2. RVE based constitutive model

The mathematical model of DPF corresponds to piece-wise description of stress strain serrations (Fig. 1) and reflects four stages distinguished within single serration: (1) elastic loading, (2) plastic loading, (3) drop of stress at constant strain, and (4) stress relaxation. Given the complex nature of single serration, it is not possible – to the knowledge of the authors – to describe the serration by means of single set of equations because of different physical mechanisms that accompany each stage of serration. Therefore, to describe stage (1) classical linear elasticity is used (equilibrium equations, Cauchy equations, constitutive law for linear elasticity). As soon as the yield surface is reached, smooth plastic flow takes place and it is reflected by the mathematical model of rate independent plasticity (constitutive law does not depend on the strain rate). Apart from classical equilibrium equations, the model includes constitutive equation and a differential equation to compute the plastic strain increment based on the associated flow rule. Here, the yield surface constitutes potential function for the plastic strains. In addition, the model is completed by the consistency condition, that means a differential equation that assures that the "working point" in the stress space remains on the yield surface. One of the crucial components of the model is mixed nonlinear hardening, that means a set of equations that describe the way the yield surface expands and moves in the stress space. These equations are based on a specific modification of classical linear

hardening, including two effects: interaction of dislocations with the inclusions and algorithm of homogenization. In both cases, a nonlinear correction of the differential equations specifying evolution of the yield surface (motion and expansion) has been made. In the part related to homogenization, a linearized tangent stiffness operator is used in order to compute the stress increment as a function of the strain increment. Generally, a boundary value problem is solved, involving set of differential equations, accompanied by suitable boundary conditions. The third stage (3) reflects drop of stress at constant total strain. Here, again, set of equations of linear elasticity, related to elastic unloading, is solved. An assumption of constant total strain has been made, which implies that the increment of plastic strain is equal to the decrement of elastic strain during unloading. The plastic strain computed from this equation corresponds to the amount of slip during the serration. Finally, during the fourth stage (4) the stress relaxation is computed. It is based on a similar mathematical model like in the case of strain rate sensitivity, with the stress reaching an asymptotic level in the course of relaxation. The process is driven by temperature, and a simple set of differential equations is solved. The mathematical model usually operates on the sets of first order differential equations, accompanied by classical algebraic equations to formulate such components of the model like the yield surface. The mathematical model is formulated in the present section, whereas its numerical implementation, allowing to follow the way the equations are integrated, is discussed in Chapter 4.

Building DPF model starts from the kinetics of formation of the lattice barriers. To this end it has been assumed that function $B$, reflecting density of the pile-ups of dislocations at the lattice barriers, depends on the accumulated plastic strain (the Odqvist parameter) in the following way [39]:

$$\partial_p B = F_B^+(\rho, T, \sigma_{ij}) H(p - p_B) \tag{7}$$

where $F_B^+$ is function of the dislocations density $\rho$, the temperature $T$ and the stress $\sigma_{ij}$. Also, $H$ denotes the Heaviside function, and $p_B$ is the threshold, expressed in terms of the accumulated plastic strain:

$$p = \int_0^{\bar{t}} \sqrt{\frac{2}{3} \dot{e}_{ij}^p \dot{e}_{ij}^p} \, dt \tag{8}$$

and dot means time derivative. Thus, the production rate of the lattice barriers is proportional to the accumulated plastic strain rate, which means that for monotonic or cyclic loading the number $B$ of produced barriers is function of the history of the process.

Another important parameter, associated with the accumulation of dislocations on the lattice barriers, is the average shear stress at the head of dislocation pile-up. In order to compute the resolved shear stress $\tau$, associated with the amount of crystallographic slip $\gamma$, it is first assumed that the evolution of dislocation density $\rho$ is described by the following equation:

$$\partial_\gamma \rho = \partial_\gamma \rho|_+ + \partial_\gamma \rho|_- \tag{9}$$

where the rate of production of dislocations is denoted by "+", whereas, the rate of annihilation of dislocations is denoted by "-" (after [18,23]). The production of dislocations is expressed by the following formula:

$$\partial_\gamma \rho|_+ = (\lambda b)^{-1} \tag{10}$$

where $\lambda$ stands for the mean free path of dislocation, and $b$ denotes the Burgers vector. The annihilation part is expressed by:

$$\partial_\gamma \rho|_- = -k_a \rho \tag{11}$$

where $k_a$ is the dislocation annihilation constant. In order to compute the mean free path of dislocations, the following rule is implemented [39]:

$$\lambda^{-1} = \sum_i \lambda_i^{-1} \Rightarrow \lambda^{-1} = d^{-1} + k_1 \sqrt{\rho} \tag{12}$$

where $d$ denotes the average size of the grains, whereas, $k_1$ is a constant. Developing Eq. (9) one obtains:

$$\partial_\gamma \rho = (db)^{-1} + k_1 \sqrt{\rho} b^{-1} - k_a \rho \tag{13}$$

Now, the Taylor factor $M$ is used, which reflects the average relation between the local microscopic shear strain or the resolved shear stress, and the global strain or stress, respectively:

$$\varepsilon = M^{-1} \gamma; \sigma = M \tau \tag{14}$$

Finally, assuming that $\varepsilon \approx \varepsilon^p$ (total strain is approximated with its plastic part only), the following formula is obtained [40]:

$$\partial_{\varepsilon^p} \rho = M\left[(db)^{-1} + k_1 \sqrt{\rho} b^{-1} - k_a \rho\right] \tag{15}$$

or, in more general form:

$$\partial_p \rho = M\left[(db)^{-1} + k_1 \sqrt{\rho} b^{-1} - k_a \rho\right] \tag{16}$$

The average shear stress in the lattice is determined by the following equation:

$$\tau_{av} = \tau_0 + \mu \alpha b \sqrt{\rho} \tag{17}$$

where $\mu$ denotes the shear modulus, and $\alpha$ reflects the interaction of dislocations [21]. Eventually, the shear stress at the head of dislocation pile-up is computed:

$$\tau_e = \pi (1 - \nu)(\mu b)^{-1} \bar{\Lambda} \tau_{av}^2 \tag{18}$$

where $\nu$ denotes the Poisson ratio and the mean free path of dislocation $\bar{\Lambda}$ contains the contribution of three types of obstacles: the grain boundaries, the dislocations and the lattice barriers [40]:

$$(\bar{\Lambda})^{-1} = d^{-1} + k_1 \sqrt{\rho} + k_2 \sqrt{B} \tag{19}$$

As the failure of the internal lattice barriers is determined by the pair of variables $(B, \tau_e)$, the following threshold function is postulated [39,40]:

$$\begin{cases} \tau_e \leq \tau_{min} \Rightarrow B = B_{cr} \\ B \leq B_{min} \Rightarrow \tau_e = \tau_{cr} \\ \tau_e > \tau_{min} \wedge B > B_{min} \Rightarrow F(B, \tau_e) = 0 \end{cases} \tag{20}$$

where function $F$ takes the following linear form:

$$F(B, \tau_e) = (B - B_{min})(\tau_{min} - \tau_{cr}) - (B_{cr} - B_{min})(\tau_e - \tau_{cr}) \tag{21}$$

Thus, $B$ and $\tau_e$ act as the variables to trigger serration. However, it has been assumed, that for sufficiently large value of one of them, the serration will occur regardless of the other:

$$B_{min}/B_{cr} = \alpha_B; \tau_{min}/\tau_{cr} = \alpha_\tau \tag{22}$$

It is now assumed, that as soon as the pair of variables $(B, \tau_e)$ reaches the above threshold function, the process of collective failure of the internal lattice barriers takes place, and all the barriers are instantaneously removed. The serration is accompanied by the drop of stress, computed in the following way [41]:

$$\Delta \sigma_{eqv}^{serr} = M \mu \alpha b \left(\sqrt{\rho^{serr}} - \sqrt{\rho}\right) \tag{23}$$

where, $\rho^{serr}$ denotes density of dislocations after drop of stress. The drop of stress is apportioned to the principal stress directions according to the following rule [41]:

$$\frac{\Delta \sigma_J^{serr}}{\Delta \sigma_K^{serr}} = \frac{\sigma_J}{\sigma_K}; \; J, K = 1, 2, 3 \; and \; J \neq K \tag{24}$$

Now, the macroscopic slip (two lattice portions being unloaded, Fig. 1) has the following magnitude:

$$\Delta \varepsilon_I^{p,serr} = -\frac{1}{E}\left[\Delta \sigma_I^{serr} - \nu\left(\Delta \sigma_J^{serr} + \Delta \sigma_K^{serr}\right)\right]$$

where

$$I, J, K = 1, 2, 3 \; and \; I \neq J \neq K \tag{25}$$

Thus, it is essentially assumed that the plastic deformation is decomposed into two parts: the plastic flow based on redistributed motion of dislocations in the lattice, represented by the accumulated plastic strain

**Table 1**
Chemical composition of grade 304 ss specimen.

|        | C      | Si     | Mn     | P     | S    | Cr        | Ni       |
|--------|--------|--------|--------|-------|------|-----------|----------|
| 304 ss | ≤ 0.07 | ≤ 0.80 | ≤ 2.00 | 0.045 | 0.03 | 17.0-19.0 | 9.0-11.0 |

$p$, and the above explained macroscopic slip, resulting from massive failure of lattice barriers, represented by the slip strain $\Delta \varepsilon_I^{p,serr}$. In order to compute the contribution related to the smooth plastic flow, the classical rate independent plasticity is used:

$$\sigma_{ij} = E_{ijkl}\left(\varepsilon_{kl} - \varepsilon_{kl}^p\right) \tag{26}$$

The potential function for plasticity is identical with the yield function:

$$f_y\left(\sigma_{ij}, X_{ij}, R\right) = \sigma_i - \sigma_y - R$$

$$\sigma_i^2 = \frac{3}{2}\left(s_{ij} - X_{ij}\right)\left(s_{ij} - X_{ij}\right) \tag{27}$$

where, $s_{ij}$, $X_{ij}$ denote the deviatoric stress and the back stress, whereas, $\sigma_y$, $R$ denote the yield stress and the isotropic hardening variable, respectively. The yield condition and the consistency condition are as follows:

$$f_y\left(\sigma_{ij}, X_{ij}, R\right) = 0; df_y = 0 \tag{28}$$

For the classical smooth plastic flow, based on redistributed motion of dislocations, the associated flow rule is assumed:

$$\partial_{\lambda^p}\varepsilon^p = n_{ij} = \partial_{\sigma_{ij}}f_y \tag{29}$$

where, $n_{ij}$, $\lambda^p$ denote the vector normal to the yield surface and the time-like parameter, respectively. The mixed hardening model contains essentially of two components: the kinematic and the isotropic hardening. The relevant evolution laws are as follows [40]:

$$\partial_{\varepsilon_{ij}^p}X_{ij} = \frac{2}{3}C_X; \partial_p R = C_R \tag{30}$$

where $C_X$, $C_R$ are the kinematic and the isotropic hardening moduli, respectively. During single serration, the pair of variables $(B, \tau_e)$ is computed in the course of smooth plastic flow (Fig. 1, stage 2), and as soon as the conditions of drop of stress are fulfilled (Eq. 20), the macroscopic slip takes place (stage 3). Finally, as indicated in Fig. 1, the drop of stress occurs at constant total strain and – thanks to the elastic unloading of the slipping portions of the continuum – the amount of macroscopic slip is determined, and a new equilibrium at lower stress level is reached.

## 3. Experimental validation of the constitutive model

In the present study, grade 304 austenitic stainless steel was examined. This material is often used for structural components working in the cryogenic conditions (down to the temperature of superfluid helium). In the near - 0K regime, grade 304 stainless steel preserves required physical and mechanical properties, including ductility. This grade is also cheaper when compared to the other grades massively used at cryogenic temperatures, like 304L, 316L, 316LN, 316 Ti, etc. On the other hand, it represents enhanced level of metastability and shows rather intensive fcc-bcc phase transformation. Therefore, application of this material is often a question of trade-off between the cost and the risk of massive strain induced phase transformation.

Two types of loading tests were performed: displacement control during uniaxial tensile test and combined tension and torsion. The chemical composition of the specimens is listed in Table 1.

Cryogenic tensile tests were performed at the liquid helium temperature (4.2 $K$), and – for comparison - at room temperature. The mechanical testing at extremely low temperatures implies application of specific cryogenic devices. For both types of test, the cryostat remains at the
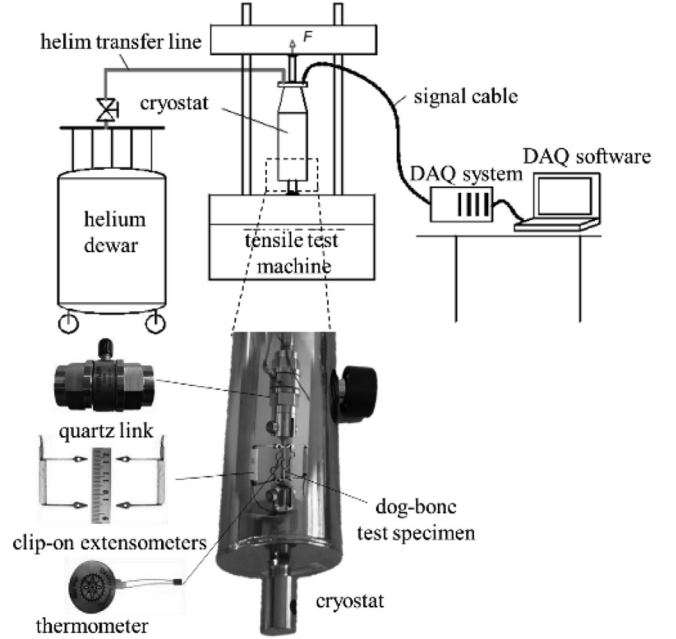


**Fig. 2.** Experimental set-up for kinematically controlled uniaxial tensile tests at 4.2 $K$: cryostat, mounted in the test machine, and equipped with suitable instrumentation: quartz link, clip-on extensometers, thermometer and specimen (Fig. 11). The transducers are connected to DAQ system.

heart of the system (vacuum insulated enclosure). It is connected to the liquid helium dewar by means of helium transfer line. Before starting any test, liquid helium flows from the dewar to the cryostat, until the specimen - equipped with multiple sensors - is entirely immersed in the cryogenic medium. The cryostat is mounted in the grips of tensile test machine that performs kinematically controlled loading (Fig. 2). The stiffness of the test set-up affects the DPF phenomenon, therefore, all tests were performed by means of very stiff Instron TT.

### 3.1. Kinematically controlled uniaxial tensile test

Kinematically controlled tensile tests (by means of bench displacement) were conducted at room and at liquid helium temperature (4.2 $K$), with the rate of 0.1 $cm/min$. The experimental set-up for tensile tests at cryogenic temperatures is shown in Fig. 2.

Flat dog bone specimens were fabricated from the commercial stainless steel (sheet) with the tensile axis in the rolling direction. The gauge length of the specimen is 20 $mm$, with the cross-section of 1.5 $mm^2$. The clip-on extensometers were used to measure the specimen elongation and the nominal strain. In order to hold the extensometers, two bronze springs were used. It is worth pointing out, that the material instability (DPF) during the uniaxial tensile test has dynamic character and may generate the oscillations of the extensometer-specimen kit. It can lead to incorrect interpretation of the test results. Therefore, the authors (2015) proposed simple approach to determine dynamic properties of the compound structure that consists of the strain gauge clip-on extensometers (dual extensometers) and the specimen. Based on this approach, the appropriate clip-on extensometers were selected to perform kinematically
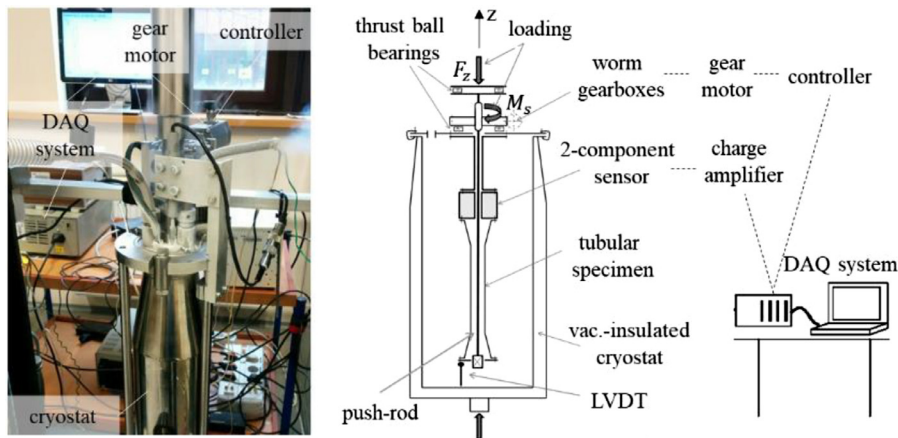
**Fig. 3.** Experimental set-up for the combined loads at 4.2 K. Tubular specimen (Fig. 11) under tension ($F_z$) and torsion ($M_s$).

**Table 2**
Experimental loading conditions.

| Loading path (programs) | Test conditions | | | |
| --- | --- | --- | --- | --- |
| | Controlled displacement $V_T$ [mm/min] | Period $t$ [s] | Controlled rotation $\omega$ [RPM] | Period $t$ [s] |
| (1) | 0.5 | 0-230 | 0.058 | 112-300 |
| (2) | | 0-183 | | 20-183 |
| (3) | | 57-180 | | 0-180 |

controlled tensile tests at 4.2 *K* for the austenitic stainless steel specimens.

A piezoelectric sensor, mounted in the cryostat just behind the specimen, was used to measure the applied force. The reference measurements of the force were carried out by external load cell. In order to measure temperature of the specimen, a thermistor was fixed directly onto the specimen. Time response of the transducers was recorded at the sampling rate of 1 *kHz*.

### 3.2. Kinematically controlled tests under combined loads

The experimental set-up for combined loads at 4.2 *K* is shown in Fig. 3. The response of the thin-walled tubes (fabricated from commercially available 304 ss tubes) under kinematically controlled tension and torsion was measured at the liquid helium temperature (4.2 *K*) in the standard testing machine, equipped with on purpose designed torsion loading device (Fig. 3). The engine transmits by means of a worm gearbox the axial force (traction) and the torque to the end of the tubular specimen (tension-torsion). The upper part of the specimen is fixed to a multiaxial force sensor that measures the compression and the tensile forces as well as the torque, applied around the spatial axis Z (Fig. 3). A commercially available piezoelectric force transducer, capable of measuring simultaneously the axial force and the torque, was used. This type of transducer has been successfully applied at CERN [40], or at Karlsruhe Institute of Technology [26]. The transducer has been calibrated for the temperature of liquid helium (4.2 K). The multiaxial force transducer is anchored to the cover plate of the cryostat.

The force in *Z* direction and the torque were used to calculate the average axial and shear stresses (see Fig. 5c, d). The instruments were connected to the data acquisition (DAQ) system. The tests were performed for various loading paths (Table 2), under displacement and rotation control. The loading rates listed in Table 2 were identified as the rates of actuator movements during the experiments. The loading paths are schematically illustrated in Fig. 5a – 7 a. The time response of the transducers was recorded at the sampling rate of 1 *kHz*.

The purpose of these tests is as follows: (1) checking the DPF under combined loads; (2) verifying the distribution of the serrations; (3) verifying the hypothesis that intensive torsion moderates the abrupt drop

of stress under combined loads; (4) identifying the parameters of the multiaxial constitutive model of DPF.

### 3.3. Test results under uniaxial traction

In this section the results of kinematically controlled uniaxial tensile tests are briefly reported. For more precise description and analysis see Skoczeń et al. [40,41] and Tabin et al. [45–47]. Fig. 4 shows typical nominal stress-strain curves, obtained for grade 304 ss flat dog bone specimens, subjected to tension at 4.2 *K* and at room temperature (RT).

It is worth pointing out, that in the near-0 K regime the stainless steel specimens preserve suitable physical and mechanical properties, including ductility. Thermodynamic conditions of DPF are strictly linked to the so-called thermodynamic instability, related to the vanishing specific heat when the temperature approaches absolute zero. The macroscopic character of DPF is reflected by the stress oscillations w.r.t. time or strain. Moreover, during the tensile tests of grade 304 stainless steel, the plastic strain induced phase transformation is observed [28,47]. Spencer et al. [42] have shown, that the martensitic transformation in the austenitic stainless steels is observed from the initial stage, and "propagates" along the tensile direction as a pseudo-Lüders front (flat part in the stress-strain curve at 4.2 *K*).

During the tensile tests of grade 304 stainless steel, the first shear band usually occurs near one of two grips (stress concentration effect). Then the shear band "propagates" across the gauge length to the second grip. Tabin et al. [45], based on special experimental set-up, identified the parameters of shear band "propagation" during kinematically controlled uniaxial tensile test in 304 stainless steel at 4.2 *K*. The "propagation" is understood here as the process of sequential formation of the shear bands one by one, and next to each other. As soon as a shear band is "locked", another shear band is formed next to the previous one and becomes active. The way of shear bands formation and "propagation" during the uniaxial tensile tests at cryogenic temperatures was presented by Tabin et al. [45] and Spencer et al. [42]. It is worth pointing out, that the apparent velocity of the shear band is correlated to the specimen thickness [6]. As soon as the front passed through the gauge length of the specimen, strong hardening has been observed. It means, that during the uniaxial tensile test the plastic flow instability is combined with the phase transformation [47]. Therefore, the following question arises:
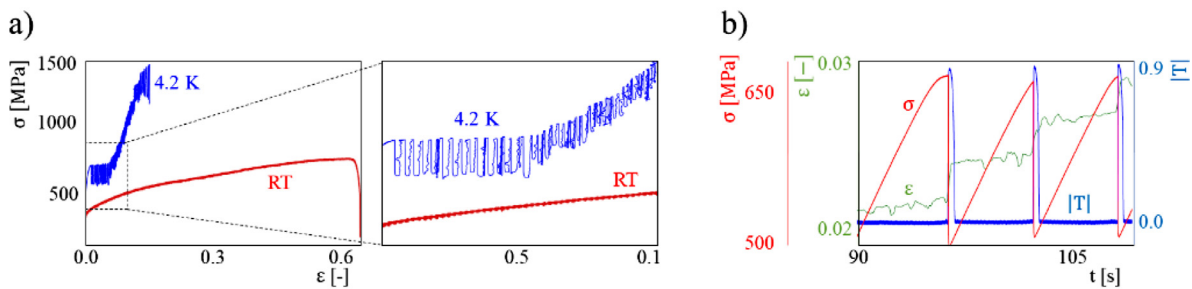
**Fig. 4.** a) Engineering stress $\sigma$ vs. engineering strain $\epsilon$ for uniaxial tensile tests of grade 304 ss for a wide range of temperatures (4.2 K and room temperature); b) time response of engineering stress (red), engineering strain (green) and normalized temperature $|T|$ (blue) at 4.2 K.
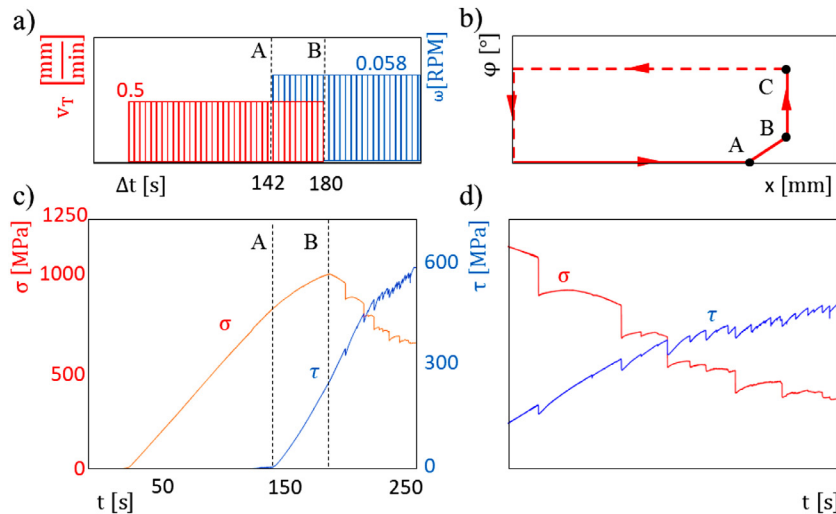


**Fig. 5.** Results of kinematically controlled combined test at 4.2 $K$ for grade 304 ss tubes; a) velocity of the test machine actuator for tension $V_T$ and torsion $\omega$ in time domain, b) program (1) of kinematically controlled loading path (A, B, C spatio-temporal points), c), d) test results: axial (red) and shear (blue) stresses w.r.t. time.

how the shear bands propagate in the course of DPF in the context of combined loads? In order to answer this question, a campaign of unique tests at 4.2 $K$ was carried out.

### 3.4. Test results under combined tension and torsion

The specimen under combined loads - tension and torsion at 4.2 $K$ - shows different types of response. Fig. 5 presents the results of a series of combined tests for grade 304 ss tubes under initial tension with the rate of $V_T = 0.5$ $mm/min$, and then, after 112 $s$, the kinematically controlled torsion with the rate of $\omega = 0.058$ $RPM$. The kinematically controlled tension has been stopped at 180 $s$, and then, only torsion was applied. Fig. 5c, d presents the nominal axial and shear stresses, calculated by means of the time response of multi-axial force transducer. Analysis of response of tube specimen subjected to combined state of stress raised the question about the initiation of plastic flow. During kinematically controlled uniaxial tension, the transition from elastic to plastic regime takes place when the yield stress is reached. In the complex, multiaxial stress state the plastic strains begin to develop in the material as soon as the yield surface is reached. One of the consequences is a decrease of axial stress, while the shear stress constantly increases (Fig. 5c). Moreover, when the plastic deformation takes place, the serrations are observed for both transducer's components.

Fig. 6 presents the results of test during which the kinematically controlled tension (which assures structural stability) is initially used, and then, after 20 $s$, the kinematically controlled torsion is initiated. The test is continued until the rupture of the specimen. In this case, the serrations are recorded by means of both components of the transducer (traction and torsion).

In order to verify the hypothesis that intensive torsion moderates the abrupt drop of stress during combined conditions, special loading paths were designed (Fig. 7b). Kinematically controlled torsion was initially applied, and then, after 57 $s$, kinematically controlled traction was initiated. In this case, the serrations related to DPF were vanishing. During this loading path, initial torsion activates plastic shear planes in the whole gauge volume, unlike for the loading paths with initial tension, where strong strain localization is observed (cf. Fig. 6c).

These test results clearly demonstrate the following deformation features of tubular specimens when the loading path changes from tension to torsion: (1) strain localization is observed for pure tension, (2) initially applied torsion activates all shear bands along the gauge length of the specimen, (3) correlation between the amplitudes of the axial and the shear stresses is observed, (4) traction stabilizes the behaviour of thin-walled sample during combined loading.

For what concerns the fracture conditions, the stainless steels of 300-series are known for low-temperature ductility. Therefore, usually ductile fracture occurs and manifests itself by the presence of dimples created by nucleation, growth, and coalescence of voids. Even in the case of massive phase transformation in the vicinity of macro-crack tip, the fracture is of ductile nature. In some specific cases, the embrittlement may take place. For example, when the solution treatment temperature in wrought steels is incorrect, fully austenitic structure will not be reached. In such a case, a multiphase steel, containing substantial amount of ferrite, may show brittle fracture. It is worth pointing out however, that the intensive martensitic transformation does not necessarily imply brittle fracture. Typically, ductile (dimpled) fracture occurs in 300-series stainless steels at 4.2 K, whereas, brittle (cleavage) fracture has not been massively observed, even if locally the amount of secondary phase generated by the strain localization may reach 100%. Grade 304 stainless steel seems to follow the same rule, therefore mostly ductile fracture has been observed.
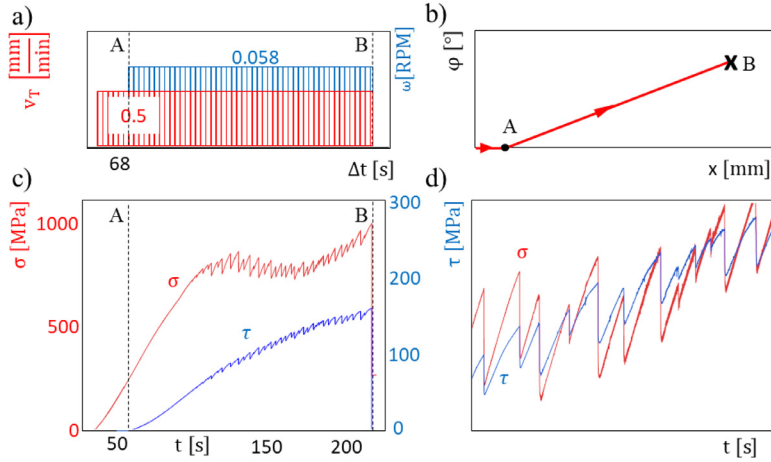
**Fig. 6.** Results of kinematically controlled combined test at 4.2 $K$ for grade 304 ss tubes; a) velocity of the test machine actuator for tension $V_T$ and torsion $\omega$ in time domain, b) program (2) of kinematically controlled loading path (A, B, C spatio-temporal points), c), d) test results: axial (red) and shear (blue) stresses w.r.t. time.
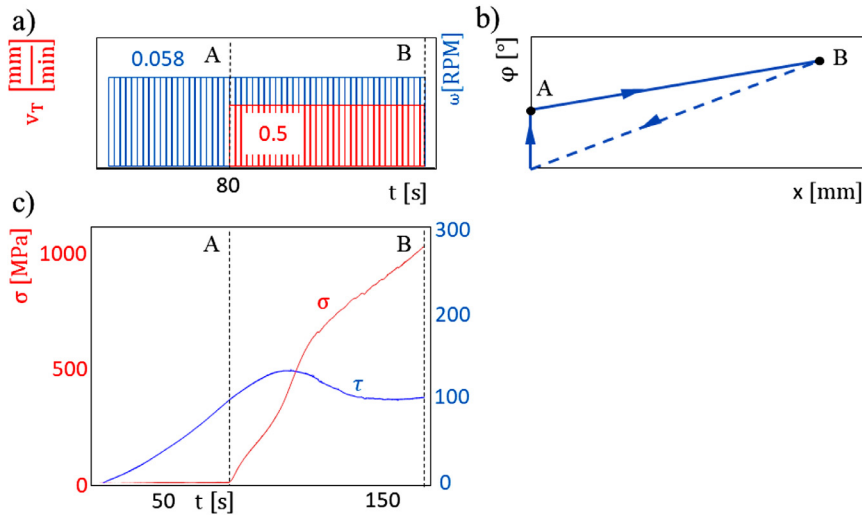


**Fig. 7.** Results of kinematically controlled combined test at 4.2 $K$ for grade 304 ss tubes; a) velocity of the test machine actuator for tension $V_T$ and torsion $\omega$ in time domain, b) program (3) of kinematically controlled loading path (A, B, C spatio-temporal points), c), d) test results: axial (red) and shear (blue) stresses w.r.t. time.

## 4. Computational aspects of the plane stress DPF

Explicit incremental scheme has been applied for integration of stresses, controlled by means of the constant value of total Cauchy strain increment $\Delta\varepsilon$, and total shear strain increment $\Delta\gamma$.

Integration starts with zero values of: the macroscopic Cauchy strain $\varepsilon$, the normal stress $\sigma$, the macroscopic shear strain $\gamma$, the shear stress $\tau$ and the out-of-plane Cauchy strain $\varepsilon_z$. Also, zero values of the plastic Cauchy strain $\varepsilon^p$, the plastic shear strain $\gamma^p$, and the plastic out-of-plane Cauchy strain $\varepsilon_z^p$ are assumed. Hence, the initial value of the Odqvist parameter $p$ is equal to zero, too. Also, the serration Odqvist parameter $p^{serr}$ (the part of plastic strain intensity corresponding to the serration-induced plastic strain) is equal to zero. The initial values of the density of lattice barriers $B = B_0$ and the density of dislocations $\rho = \rho_0$ are set. It is worth pointing out that the thin-walled tubes and the flat dog bone specimens were, respectively, fabricated from the commercial stainless steel bar and the commercial sheet with the tensile axis in the rolling direction. However, the texture induced anisotropy has not been taken into account. The threshold of the Odqvist parameter for the onset of the lattice barriers evolution $p_B = p_{B0}$ is introduced.

In what follows, $E$ denotes the Young modulus and $\mu = \frac{E}{2(1+\nu)}$ (with $\nu$ standing for the Poisson ratio) denotes the shear modulus for virgin material. Starting value for the macroscopic yield stress $\sigma_y = \sigma_{y0}$ is assumed.

As long as the stresses remain inside the yield surface (stage 1 of single serration), the strains and the stresses are updated in the following way:

$$\varepsilon \leftarrow \varepsilon + \beta\Delta\varepsilon, \gamma \leftarrow \gamma + \beta\Delta\gamma, \tag{31}$$

$$\sigma \leftarrow \sigma + \beta E\Delta\varepsilon, \tau \leftarrow \tau + \beta\mu\Delta\gamma. \tag{32}$$

The increment-scaling parameter $\beta$ is always equal to 1, except for the last step of elastic deformation range, after the yield surface is exceeded, i.e. if:

$$(\sigma + E\Delta\varepsilon)^2 + 3(\tau + \mu\Delta\gamma)^2 > \left(\sigma_y(p)\right)^2 \tag{33}$$

then $\beta$ is changed for:

$$\frac{-(2E\sigma\Delta\varepsilon + 6\mu\tau\Delta\gamma) + \sqrt{(2E\sigma\Delta\varepsilon + 6\mu\tau\Delta\gamma)^2 - 4\left[(E\Delta\varepsilon)^2 + 3(\mu\Delta\gamma)^2\right]\left(\sigma^2 + 3\tau^2 - \sigma_y^2\right)}}{2\left[(E\Delta\varepsilon)^2 + 3(\mu\Delta\gamma)^2\right]} \tag{34}$$

in order to move the stress point back onto the yield surface. After the strains and the stresses are updated with the use of Eq. (31) and Eq. (32), the out-of-plane strain is calculated:

$$\varepsilon_z = \frac{1}{2}\left(\frac{1-2\nu}{E}\sigma - \varepsilon\right) \tag{35}$$

and - besides them - none of the state parameters changes, but the continuous plastic flow starts (stage 2). During this process the strains are updated according to Eq. (31) (with $\beta = 1$), and the predictor-corrector

scheme is used to update the stresses. First, the elastic predictor for the stresses is calculated:

$$\sigma^* = \sigma + E\Delta\varepsilon, \tau^* = \tau + \mu\Delta\gamma, \tag{36}$$

the plastic multiplier $\Delta\lambda$ is assumed to be zero, and the iterative procedure (corrector) starts in order to establish new values of the stresses and the plastic multiplier:

$$\sigma = \sigma^*/(1 + 2E\Delta\lambda), \tau = \tau^*/(1 + 6\mu\Delta\lambda) \tag{37}$$

$$\Delta\varepsilon^p = \Delta\lambda \cdot 2\sigma, \Delta\gamma^p = \Delta\lambda \cdot 6\tau \tag{38}$$

$$\Delta\varepsilon_z^p = \sigma/(2E) - \varepsilon/2 - \varepsilon_z^p \tag{39}$$

the increment of the Odqvist parameter:

$$\Delta p = \sqrt{(\Delta\varepsilon^p)^2 + \frac{1}{2}(\Delta\gamma^p)^2 + 2(\Delta\varepsilon_z^p)^2} \tag{40}$$

finally, the difference between new stress intensity and new yield stress reads:

$$\delta(\Delta\lambda) = \sqrt{\sigma^2 + 3\tau^2} - \sigma_y(p + \Delta p) \tag{41}$$

As long as $\delta \neq 0$ (in practice, $|\delta|$ is not sufficiently small), the procedure is looped back to Eq. (37) after correction of $\Delta\lambda$ using the Newton method:

$$\Delta\lambda \leftarrow \Delta\lambda - \frac{\delta}{\delta'} \tag{42}$$

Here, $\delta'$ stands for the derivative $\mathrm{d}\delta/\mathrm{d}(\Delta\lambda)$, approximated by the forward finite difference scheme:

$$\frac{\mathrm{d}\delta}{\mathrm{d}(\Delta\lambda)} \cong \frac{\delta(\Delta\lambda + \Delta(\Delta\lambda)) - \delta(\Delta\lambda)}{\Delta(\Delta\lambda)} \tag{43}$$

Equations (37) through (41), with $\Delta\lambda$ substituted by $\Delta\lambda + \Delta(\Delta\lambda)$, are used to calculate the first component of the numerator in Eq. (43). The current value of the yield stress $\sigma_y$ is calculated for linear isotropic hardening, with the hardening modulus $E_h$:

$$\sigma_y(p) = \sigma_{y0} + E_h(p - p^{serr}) \tag{44}$$

After the iteration process is completed, the stress components as well as the total strain components are known, and the out-of-plane strain component is calculated using Eq. (35). The plastic parts of the strains are updated:

$$\varepsilon^p \leftarrow \varepsilon^p + \Delta\varepsilon^p, \gamma^p \leftarrow \gamma^p + \Delta\gamma^p, \varepsilon_z^p \leftarrow \varepsilon_z^p + \Delta\varepsilon_z^p \tag{45}$$

and, hence, the Odqvist parameter is updated, too:

$$p \leftarrow p + \Delta p \tag{46}$$

The threshold is then checked with respect to the evolution of lattice barriers. If it is reached, the evolution goes on:

$$\text{if } p \geq p_B \text{ then } B \leftarrow \min(B_{cr}, B + F_{LC}^+ \cdot \Delta p) \tag{47}$$

During the continuous plastic flow, the density of dislocations evolves:

$$\rho \leftarrow \rho + M\left(\frac{1}{db} + \frac{k_1\sqrt{\rho}}{b} - k_a\rho\right)\Delta p \tag{48}$$

and the modified average shear stress in the lattice $\tau_{av}$ can be obtained from Eq. (17). Also, the mean free path of dislocations $\bar{\Lambda}$ is calculated from Eq. (19). Finally, the average shear stress at the head of dislocation pile-ups $\tau_e$ is computed based on Eq. (18), and the serration criterion is checked - Eq. (20). If the interaction curve is not reached, the integration process is continued starting from Eq. (36). If it is reached, the serration takes place (stage 3), resulting in discontinuous change of the stresses. First, the equivalent drop of stress is computed:

$$\Delta\sigma_{eqv}^{serr} = M\mu\alpha b\left(\sqrt{\rho^{serr}} - \sqrt{\rho}\right) \tag{49}$$

with $\rho^{serr}$ being the after-serration density of dislocations, approximated experimentally by the best-fit formula:

$$\rho^{serr} = \left(\frac{0.00031}{p^{2/3}} + 0.2\right)\rho \tag{50}$$

based on tensile test results for grade 304 stainless steel at 4.2 K. Then, the serration drops of the particular stress components are computed. Namely, if the shear stress $\tau = 0$, then:

$$\Delta\sigma^{serr} = \sigma_y(p) + M\mu\alpha b\left(\sqrt{\rho^{serr}} - \sqrt{\rho}\right) - \sigma, \Delta\tau^{serr} = 0 \tag{51}$$

If $\sigma = 0$, then:

$$\Delta\tau^{serr} = \frac{\sqrt{3}}{3}\left[\sigma_y(p) + M\mu\alpha b\left(\sqrt{\rho^{serr}} - \sqrt{\rho}\right)\right] - \tau, \Delta\sigma^{serr} = 0 \tag{52}$$

If both $\sigma \neq 0$ and $\tau \neq 0$, then it is postulated that the components of drop of stress are proportional to the current stress values (Eq. (24)):

$$\frac{\Delta\sigma^{serr}}{\Delta\tau^{serr}} = \frac{\sigma}{\tau} \tag{53}$$

Hence

$$\Delta\tau^{serr} = \frac{\tau}{\sigma}\Delta\sigma^{serr} \tag{54}$$

and $\Delta\sigma^{serr}$ is computed as the root of the nonlinear equation:

$$\sqrt{(\sigma + \Delta\sigma^{serr})^2 + 3\left(\tau + \frac{\tau}{\sigma}\Delta\sigma^{serr}\right)^2} - \sigma_y(p) - M\mu\alpha b\left(\sqrt{\rho^{serr}} - \sqrt{\rho}\right) = 0 \tag{55}$$

The bisection method is effectively applied, and the root is sought for in the interval:

$$-\sigma < \Delta\sigma^{serr} < 0 \tag{56}$$

Having the stress decrements calculated, and recalling the observation of constant value of the total strain during serration, which implies that the increment of the plastic strain is equal to the decrement of its elastic part, eventually, the total strain values $\varepsilon$ and $\gamma$ (and also $\varepsilon_z$) are kept unchanged, whereas the serration-induced increments of their plastic parts are expressed as:

$$\Delta\varepsilon^{p, serr} = -\frac{\Delta\sigma^{serr}}{E}, \Delta\gamma^{p, serr} = -\frac{\Delta\tau^{serr}}{\mu}, \Delta\varepsilon_z^{p, serr}$$
$$= \left(\frac{1 - 2\nu}{E}\Delta\sigma^{serr} - \Delta\varepsilon^{p, serr}\right)/2 \tag{57}$$

This allows to compute the serration increment of the Odqvist parameter:

$$\Delta p^{serr} = \sqrt{(\Delta\varepsilon^{p, serr})^2 + \frac{1}{2}(\Delta\gamma^{p, serr})^2 + 2(\Delta\varepsilon_z^{p, serr})^2} \tag{58}$$

and the plastic strains increase to:

$$\varepsilon^p \leftarrow \varepsilon^p + \Delta\varepsilon^{p, serr}, \gamma^p \leftarrow \gamma^p + \Delta\gamma^{p, serr}, \varepsilon_z^p \leftarrow \varepsilon_z^p + \Delta\varepsilon_z^{p, serr} \tag{59}$$

with the Odqvist parameter, as well as the serration Odqvist parameter, changed to:

$$p \leftarrow p + \Delta p^{serr}, p^{serr} \leftarrow p^{serr} + \Delta p^{serr} \tag{60}$$

Finally, the stresses are updated:

$$\sigma \leftarrow \sigma + \Delta\sigma^{serr}, \tau \leftarrow \tau + \Delta\tau^{serr} \tag{61}$$

and then the out-of-plane strain is calculated according to Eq. (35).

At the end of the serration step (stage 3), the dislocations density is reduced to $\rho^{serr}$ (Eq. (50)), and the density of lattice barriers is significantly reduced to 102% of starting value. New threshold of the Odqvist parameter for lattice barriers evolution, $p_{LC}$, is established:

$$p_B = p + p_{B0} \tag{62}$$

and $p_{B0}$ is reduced down to $0.95 \cdot p_{B0}$ in order to model the increasing "density" of future serrations.

The relaxation phase (stage 4) starts immediately after drop of stress. Eq. (31) with $\beta = 1$ is again used for the update of total strain values, whereas the decrements of the stresses change iteratively:

$$\Delta\sigma \leftarrow (\sigma_\infty - \sigma - \Delta\sigma)/t_\Phi, \ \Delta\tau \leftarrow (\tau_\infty - \tau - \Delta\tau)/t_\Phi \qquad (63)$$

with the initial values of $\Delta\sigma$ and $\Delta\tau$ obtained as the results of Eqs (51) through (55). The stresses are updated according to:

$$\sigma \leftarrow \sigma + \Delta\sigma, \ \tau \leftarrow \tau + \Delta\tau \qquad (64)$$

and the out-of-plane strain $\varepsilon_z$ is determined due to Eq. (35). Such heuristic relations for the change of the stresses require evaluation of the strains with respect to their elastic or plastic components, with total control increments $\Delta\varepsilon$ and $\Delta\gamma$ kept unchanged. Thus, if the elastic change of any strain turns out to be less than the total strain increment, it means that this increment consists of the elastic and the plastic part. So, the following conditions apply:

$$\text{if } \left|\frac{\Delta\sigma}{E}\right| < |\Delta\varepsilon| \text{ then } \Delta\varepsilon^p = \Delta\varepsilon - \frac{\Delta\sigma}{E} \text{ else } \Delta\varepsilon^p = 0 \qquad (65)$$

$$\text{if } \left|\frac{\Delta\tau}{\mu}\right| < |\Delta\gamma| \text{ then } \Delta\gamma^p = \Delta\gamma - \frac{\Delta\tau}{\mu} \text{ else } \Delta\gamma^p = 0 \qquad (66)$$

$$\text{if } \left|\frac{\nu\Delta\sigma}{E}\right| < \left|\frac{\frac{1-2\nu}{E}\Delta\sigma - \Delta\varepsilon}{2} - \varepsilon_z\right| \text{ then } \Delta\varepsilon_z^p$$

$$= \frac{\frac{1-2\nu}{E}\Delta\sigma - \Delta\varepsilon}{2} - \frac{\nu\Delta\sigma}{E} \text{ else } \Delta\varepsilon_z^p = 0 \qquad (67)$$

The plastic parts of the strains are updated like in Eq. (45) and, eventually, the Odqvist parameter $p$ is increased by $\Delta p$, as expressed by Eq. (40).

The relaxation phase is looped to Eq. (63), with the total strain values updated each time, as long as the stresses $\sigma$ and $\tau$ become sufficiently close to their asymptotic values $\sigma_\infty$ and $\tau_\infty$, assumed to be 95% of the after-serration values obtained in Eq. (61). After the asymptotic level has been reached, the integration scheme goes back to Eq. (31), i.e. to the elastic deformation range. Note, that the serration-induced increment of the Odqvist parameter does not influence the hardening curve, as proved in the experimental data and expressed in Eq. (44), where the serration Odqvist parameter is subtracted from the total Odqvist parameter.

Since the experiments are performed with the use of cylindrical specimen of $L = 0.01 \ mm$ the length, $R = 6.185 \ mm$ the middle radius, and $g = 0.37 \ mm$ the wall thickness, and the kinematic control is applied, i.e. the elongation $u$ and the angle of twist $\phi$ are enforced, the normal force $N_f$ and the torque $M_t$ are measured as the reactions. Hence, the following relations take place between the strains and the stresses vs. the elongation, the angle of twist, the normal force and the torque:

$$\varepsilon = \frac{u}{L}, \ \gamma = \frac{\varphi R}{L} \qquad (68)$$

$$N_f = 2\pi R g \cdot \sigma, \ M_t = 2\pi R^2 g \cdot \tau \qquad (69)$$

As described in Chapter 3.4, three programs of kinematically controlled loading paths are considered for the numerical calculations (Fig. 8). Since the physical time (measured in seconds) is different for each loading path, a dimensionless step value is used for abscissa in Fig. 8 and Fig. 9. This is a time-like parameter, for which zero value denotes the start of the program, whereas value 1 stands for the end of the program.

In the first program (1), tension-only deformation is enforced due to the controlled elongation $u$, with the angle of twist $\phi$ kept zero, through the half of the test time. Then, with $u$ still increasing, the torsion starts with the controlled angle of twist $\phi$. Finally, the increase of the elongation is stopped, whereas the angle of twist increases for a short time interval. In the second program (2), the elongation $u$ monotonically in-
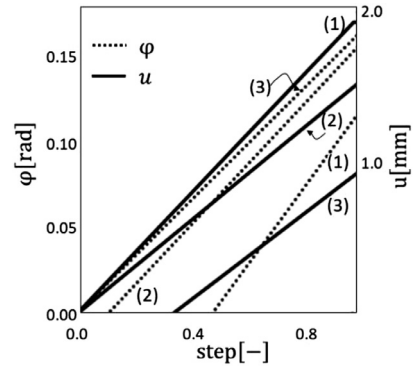


**Fig. 8.** Three programs (1), (2) and (3) of combined kinematically controlled loading paths.

creases through all time interval (with the velocity slightly lower than in (1)), and the twist starts at one tenths of the time interval and then continuously grows. The third scheme (3) exhibits initially the torsion-only deformation, with the angle of twist $\phi$ monotonically increasing through all time interval, whereas the tension starts later on due to the elongation $u$ delayed by one third of the test time.

The results of the numerical simulations are presented in Fig. 9 for each loading path, respectively. Each diagram presents the change of normal stress $\sigma$ and shear stress $\tau$ during the test time: a), d), g) entire path with the elastic part and the continuous plastic flow, followed by discontinuous (serrated) plastic flow; b), e), h) enlarged view of a portion of the equilibrium path, to illustrate the separate serrations; c), f), i) interaction curve $\tau$-$\sigma$ related to the initial yield surface, with visible plastic hardening and the serrations directed inside.

For all three loading programs, the numerically simulated data correlate to the experimental results. First, only one kinematic control parameter is active (either elongation $u$ or angle of twist $\phi$), and the deformation process runs in the elastic deformation range, followed by the continuous plastic flow with one non-zero stress component (either normal stress $\sigma$ or shear stress $\tau$). After the serration condition is satisfied (i.e. the accumulated plastic strain is big enough), the equilibrium paths enter the discontinuous plastic flow. One may also observe, that as soon as the second kinematic parameter is triggered (with some delay w.r.t. the first one), the stress connected with the first one decreases, so as to keep the stress components on the yield surface. Afterwards, as long as both control parameters keep increasing, the DPF process runs in stable form. If the increase of one parameter is stopped (the very end of loading program 1), the stress component connected with it strongly decreases, whereas the other stress component strongly increases. Again, this is because both stress components must remain on the yield surface. The numerical simulation confirms that initiation of the tension process after preceding torsion (loading program 3) stabilizes the serrations of the shear stress, i.e. the serration amplitude is significantly reduced.

Some of the parameters (Table 3) come from the cited literature positions (e.g. initial dislocation density $\rho_0$, initial density of the lattice barriers $B_0$, etc.), some of them are typical material constants ($E_h$, $\nu$, etc.). Finally, some of them come from the in-house experiments, and a few were chosen so as to correctly calibrate the model ($k_1$, $k_a$, etc.).

## 5. Discussion

In the present paper a fundamental question has been raised, whether the discontinuous plastic flow observed at extremely low temperatures is multiaxial by nature. Moreover, the mechanism of the multiaxial DPF has been experimentally and numerically investigated. The first attempt to explain the multiaxial nature of DPF has been undertaken in one of the previous papers, where during the classical uniaxial test the flat sample was initially twisted. In the course of test, the elongation of
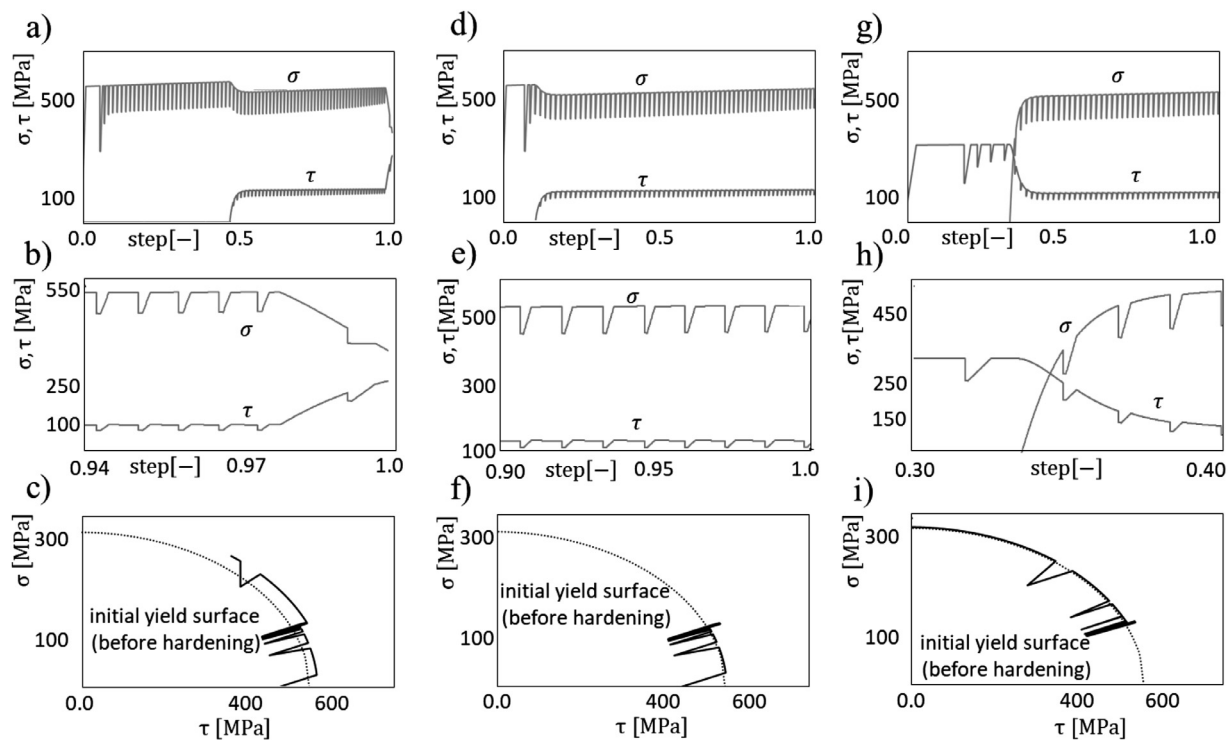
**Fig. 9.** The serrated equilibrium paths for the loading program: (1) a-c, (2) d-f, (3) g-i; entire equilibrium path a), d), g); enlarged view of a portion of the equilibrium path b), e), h); serrated interaction curve $\tau$-$\sigma$ vs. initial yield surface c), f), i).

**Table 3**
Set of parameters adopted for numerical analysis.

| parameter | | source | equation | value |
|---|---|---|---|---|
| $\tau_0$ | internal lattice friction | in-house experiments | Eq. (17), Eq. (44) | $\frac{\sigma_{p0}}{M} = \frac{550}{3}$ [MPa] |
| $\mu$ | shear modulus | in-house experiments | Eq. (32) | $\frac{E_0}{2(1+\nu)} = \frac{2.1 \cdot 10^5}{2(1+0.3)}$ [MPa] |
| $\alpha$ | dislocations interaction factor | [23] | Eq.(17) | 0.4 |
| $b$ | length of the Burgers vector | [5] | Eq. (48) | $2.58 \cdot 10^{-8}$[mm] |
| $d$ | average grain size | in-house data | Eq. (48) | $5 \cdot 10^{-4}$[mm] |
| $k_1$ | constant | in-house data | Eq. (48) | 0.25 |
| $k_2$ | constant | in-house data | Eq.(19) | 0.01 |
| $k_a$ | dislocation annihilation constant | in-house data | Eq. (48) | 0.01 |
| $t_\Phi$ | time of the relaxation process | in-house experiments | Eq. (63) | 100[s] |
| $E_h$ | hardening modulus | in-house experiments | Eq. (44) | 200[MPa] |
| $B_0$ | initial value of density of the lattice barriers | prediction (based on [5]) | | $5 \cdot 10^8 [\frac{1}{mm^2}]$ |
| $\rho_0$ | density of dislocations | prediction (based on [5]) | | $5 \cdot 10^8 [\frac{1}{mm^2}]$ |
| $p^p_{LC0}$ | initial plastic strain intensity threshold for the evolution of the lattice barriers | in-house experiments | | 0.01 |

the sample was accompanied by the evolution of the unit angle of twist, which led to the conclusion, that coexistence of both strain components (axial and shear) does not exclude the serrated yielding (Fig. 10a).

In the course of the present work, based on the unique set-up for testing thin-walled tubular specimens under tension and torsion, it has been proved that DPF is observed under biaxial stress state, and the serrations in both directions are coupled. It is worth pointing out, that the mechanism of DPF under kinematically controlled combined loads at extremely low temperatures seems to be the same when compared to uniaxial tests. In the course of plastic flow in the weakly excited lattice, the dislocations accumulate on the internal lattice barriers and form fairly stable pile-ups. As soon as the resolved shear stress at the head of dislocation pile up reaches the level of the cohesive strength of the material, the barriers are overcome, and the liberated dislocations can freely glide away. If the phenomenon is massive and has collective character, the effect becomes macroscopic and leads to rapid drop of stress, accompanied by macroscopic measurable slip. It turns out, that the slip can be accompanied by twinning, however, the contribution of twinning is not yet fully explained.

Comparison of uniaxial and multiaxial DPF reveals however quite specific features of both of them. In the uniaxial case, the lattice barriers are produced within the shear bands, that "propagate" in a discontinuous and sequential manner from one extremity of the sample (stress concentration effect) to the other. The "propagation" is understood here as the process of sequential formation of the shear bands one by one, and next to each other. As soon as a shear band is "locked", another shear band is formed next to the previous one and becomes active. This is due to the fact, that at extremely low temperatures DPF is combined with the plastic strain induced fcc-bcc phase transformation, and the shear bands are "locked" by increasing amount of secondary phase. Therefore, active slip planes contributing to a shear band are blocked in terms of free motion of dislocations, and – as a result – another shear band is sequentially created. This is the mechanism of sequential activation of the shear bands, characteristic of uniaxial state of stress [42]. On the other hand, in the thin-walled tubular samples, subjected to simultaneous traction and torsion, all cross-sections are simultaneously activated in terms of shear. This means that in all cross-sections of the sample the plastic flow takes place, and the lattice barriers are created.
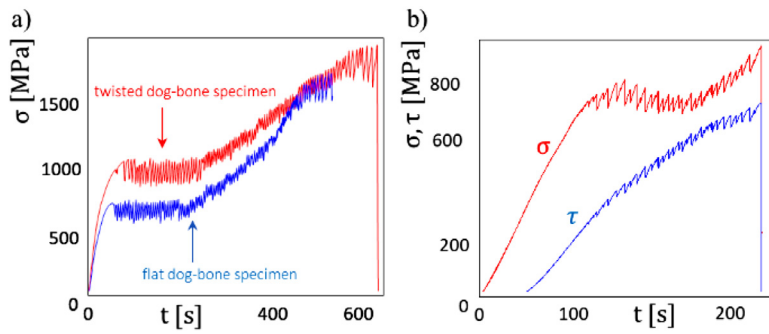
**Fig. 10.** Multiaxial DPF at 4.2K (a) engineering stress w.r.t. time during kinematically controlled uniaxial test with strain rate 0.1 *cm/min*, 304ss, twisted and flat dog-bone specimens (b) engineering axial and shear stresses w.r.t. time during biaxial test, 304ss, thin-walled tubular specimen: tension and torsion.
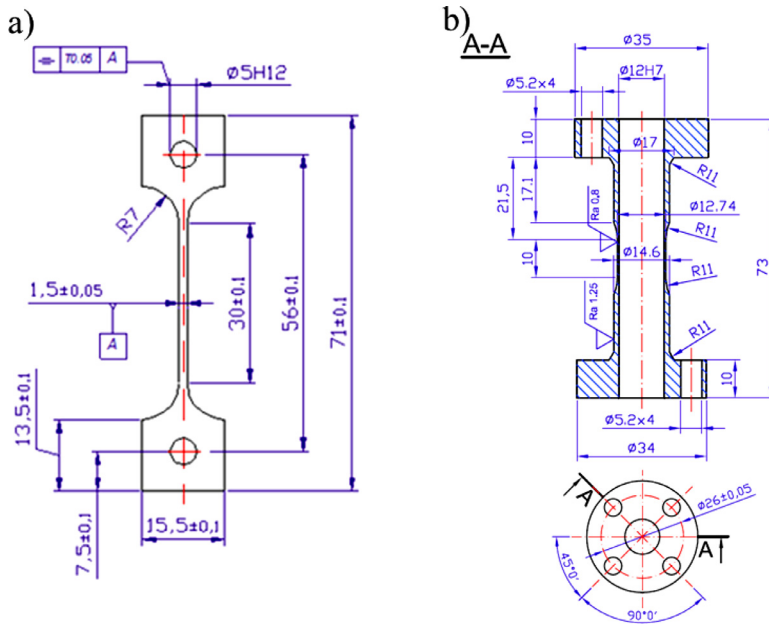


**Fig. 11.** Dog-bone specimen for uniaxial tensile test (1.5 mm thickness); b) tubular specimen for combined loading - tension and torsion.

Thus, the pile-ups of dislocations occur in all cross-sections simultaneously, and the collective effect is triggered in one of the regions of the sample, which leads to simultaneous serration in the axial and in the circumferential direction. This implies strong coupling between them, and the serration is visible in both directions: axial and angular (traction and torsion). Such interpretation is well visible in the plots shown in the Section 3.4. As the plastic flow is simultaneously initiated in all cross-sections of the sample, the stress level reached during the test of combined loads is clearly lower than in the case of the equivalent uniaxial test. This is due to the fact, that the work of the external forces on the axial and the angular displacements is redistributed between the traction and the shear, and the internal energy dissipated in both directions is fraction of the total dissipated energy. For instance, the serrations during uniaxial test may even reach some 200 *MPa*, whereas, the serrations during multiaxial test reach in the axial direction some 100 *MPa* at most, and the shear stress serrations are roughly half of the serrations in the axial direction. The constitutive model and its numerical realization reflect very well these proportions. It is worth pointing out, that both proportional (proportional increase of components of the strain rate tensor) and non-proportional (also referred as disproportional) loading paths were performed, and in the cases shown in Figs 5 and 6 the serrations were observed in either direction. Perfect synchronisation of serrations in the axial and in the angular directions indicates strong coupling between them. This backs the hypothesis, that the drop of stress in a given direction is proportional to the level of stress reached before serration, which has been embedded into the constitutive model.

In the proximity of absolute zero several thermodynamic variables like thermal conductivity and thermal contraction coefficient, or functions like specific heat and entropy tend to zero. It strongly affects the behaviour of fcc materials at near 0 K temperatures, especially for what concerns dissipative phenomena related to discontinuous plastic flow. During the abrupt drop of stress, the temperature increases as a result of conversion of plastic power to heat. The amount of heat produced during the massive rupture of lattice barriers is function of plastic power and internal friction. During the first stage of serration (elastic loading and smooth plastic flow), the heat is transported to the surrounding helium. On the other hand, during the abrupt drop of stress that lasts several micro-seconds, the heat exchange can be practically neglected (nearly adiabatic conditions), and the plastic power is entirely converted to heat. This results in temperature rise that – in the case of stainless steels – may reach some 20-30 K. Such a strong temperature increase, that resembles Dirac delta, is subjected to further relaxation due to the heat diffusion process. Nevertheless, the mechanical and the physical properties of the material are locally affected by the temperature increase, until its final decay. Generally, there is two consequences of such a thermodynamic process:

- if – because of the strain rate – the temperature increase in large fractions of the specimen exceeds the threshold $T_0/T_1$, smooth plastic flow takes place, until the temperature drops back below the threshold,
- if the increase of temperature remains local, causes local lattice excitation, and facilitates massive motion of dislocations, the stress relaxation in the final stage of serration is observed.

The stress relaxation (stage 4) has been included in the constitutive model, both in the uniaxial and the biaxial version. During the relaxation, there is usually no other significant heat source and the material is eventually cooled down to the liquid helium temperature. The problem of temperature decay and the stress relaxation has been discussed in detail in the paper by J. [45].

Generally, the constitutive model offers quite good insight into the phenomena taking place in the material (continuum) during single serration and allows to simulate the sequence of serrations in both directions. Each serration has been subdivided into 4 stages: elastic loading, smooth plastic flow, drop of stresses and relaxation. During smooth plastic flow, the number of internal lattice barriers increases, and the shear stresses at the heads of dislocation pile-ups rise. As soon as the serration criterion is fulfilled, the lattice barriers are overcome, and the drop of stress begins. During drop of stress at constant total strain, the macroscopic slip takes place and its amount is equivalent to elastic unloading of the slipping parts of the continuum. The model has been implemented and generates correct results when compared to the experiment. In particular, the serrations in both directions fit quite well to the experimental data, and the illustration of serrations w.r.t. yield surface in the $(\sigma, \tau)$ plane is qualitatively correct. Also, the proportions of the shear-to-axial serrations correspond - in most of the analysed cases - to the experimental data.

It has to be underlined, however, that the texture induced anisotropy and the plastic strain induced fcc-bcc phase transformation might affect the results. DPF is coupled to plastic strain induced fcc-bcc phase transformation, which implies evolution of microstructure in the course of inelastic deformation. The evolution of microstructure will have impact both on the grain size, as well as on the creation of additional barriers for the motion of dislocations. In the present study the above effects were not taken into account. Essentially, the sample has been treated as fully recrystallized and untextured. For the time being, the model is based on the assumption of constant grain size and lack of additional barriers in the form of nucleation of secondary phase. Thus, the TRIP effect has been ignored in the present paper, even it has been accounted for in one of the previous papers dedicated to coupling between the DPF and the phase transformation (cf. [47]). However, the model discussed in the quoted paper was uniaxial. Taking into account full coupling between the DPF and the phase transformation in the multiaxial context and including the effect of dynamic change of the grain size and the evolution of barriers resulting from nucleation of secondary phase in the course of plastic deformation, is quite complex and requires further studies involving the relevant experiments. Thus, this problem will be considered in the next version of the model.

Finally, there is one effect that needs to be highlighted. The axial stress against strain (or time) reaches its local maximum during loading, and then local softening followed by the hardening occurs. This is due to the fact, that torsion activates all the cross-sections in terms of the plastic flow, which implies local softening in the axial direction, before the hardening can restart. This effect is also observed in the classical smooth plastic flow regime, at higher temperatures or in the NiTi tubes subjected to torsion loading, where the phase transformation is activated in all cross-sections of the gauge length [35].

## 6. Conclusions

The mechanism of discontinuous plastic flow (DPF, serrated yielding), that occurs at extremely low temperatures, has been explained in the context of kinematically controlled complex loads and non-proportional loading paths. To this end, dedicated set-up consisting of a cryostat equipped with remotely controlled insert, containing thin-walled tubular sample subjected to tension and torsion has been developed. Loading program in liquid helium (4.2 K) has been stretched over the proportional and the non-proportional paths, composed of elongation (traction) and angular motion (twist). One of important limitations in the course of biaxial test was stability of specimen against buckling. In order to assure stability of thin-walled sample, the loading paths were thoroughly studied in order to avoid possible structural effects in the form of buckling.

Both for proportional and non-proportional loading paths, the DPF has been observed in each direction simultaneously (traction and torsion), and the serrations were correlated with each other, even if their amplitudes were different. The same hypothesis as for the uniaxial stress state has been maintained: the plastic flow instabilities, reflected by sudden drops of stresses, are attributed to the mechanism of formation of lattice barriers, accompanied by the pile-ups of dislocations. Catastrophic failure of barriers in the weakly excited lattice (collective effect) leads to massive motion of released dislocations, accompanied by the macroscopic slip and drop of stress. Due to conversion of plastic power to heat and the effect of adiabatic heating, each serration is accompanied by sharp rise in temperature in the form of the Dirac delta. The contribution of twinning remains still to be further investigated and explained.

Physically based multiaxial constitutive model has been built and numerically implemented. The model takes into account the characteristic features of DPF: production of lattice barriers and formation of pile-ups of dislocations, the criterion of their collective failure, and experimentally confirmed assumption of simultaneous serrations in the loading directions. It has been shown that the model is able to reproduce the observed serrations and reflects the experimental data in a qualitative manner. Also, the model keeps correct relations between the frequency and the amplitude of serrations in both loading directions (traction and torsion).

Finally, it is worth pointing out that the results of tests under combined loads (traction and torsion) in the proximity of absolute zero are for the first time reported, and these novel results confirm the assumptions accepted when building the constitutive model.

## Declaration of Competing Interest

The authors declare that they have no known competing financial interests or personal relationships that could have appeared to influence the work reported in this paper.

## CRediT authorship contribution statement

**J. Tabin:** Methodology, Validation, Investigation, Resources, Data curation, Visualization, Writing - original draft, Writing - review & editing. **B. Skoczeń:** Conceptualization, Methodology, Supervision, Resources, Writing - original draft, Writing - review & editing. **J Bielski:** Software, Formal analysis, Data curation, Resources, Writing - original draft, Writing - review & editing.

## Acknowledgements

## References

[1] Barlat F, Yoon S-Y, Lee S-Y, Wi M-S, Kim J-H. Distortional plasticity framework with application to advanced high strength steel. International Journal of Solids and Structures 2020;202:947–62.

[2] Basinski ZS. The instability of plastic flow of metals at very low temperatures. Proceedings of the Royal Society of London Series A 1957;240:229–42.

[3] Blewitt TH, Coltman RR, Redman JK. LOW-TEMPERATURE DEFORMATION OF COPPER SINGLE CRYSTALS. Journal of Applied Physics 1957;28:651–60.

[4] Bobrov VA, Lebedkin MA, Tybulewicz A. Role of dynamic processes in low-temperature jump-like deformation of aluminum. Physics of the Solid State 1993;35:939–43.

[5] Bouquerel J, Verbeken K, De Cooman BC. Microstructure-based model for the static mechanical behaviour of multiphase steels. Acta Materialia 2006;54:1443–56.

[6] Cai Y-L, Yang S-L, Fu S-H, Zhang Q-C. The Influence of Specimen Thickness on the Lüders Effect of a 5456 Al-Based Alloy: Experimental Observations. Metals 2016;6:120.

[7] Cardwell DA, Ginley DSE. Handbook of Superconducting Materials. 1st ed. CRC Press; 2002.

[8] Devred A. Practical Low-Temperature Superconductors for Electromagnets, Geneva, CERN: CERN; 2004. Monographs), C.Y.R. (Ed.).

[9] Duda A, Mangiarotti F, Bajko M, Bernhard A, Desbiolles V, Ferracin P, Feuvrier J, Fajardo LG, Lorenzo J, Mazet J, Pérez JC, Schoerling D, Willering G. Power Test of the Second-Generation Compact Linear Collider (CLIC) Nb3Sn Damping Wiggler Short Model. IEEE Transactions on Applied Superconductivity 2019;29:1–5.

[10] Estrin Y, Kubin LP. Criterion for thermomechanical instability of low temperature plastic deformation. Scripta Metallurgica 1980;14:1359–64.

[11] Garion C, Skoczeń B, Sgobba S. Constitutive modelling and identification of parameters of the plastic strain-induced martensitic transformation in 316L stainless steel at cryogenic temperatures. International Journal of Plasticity 2006;22:1234–64.

[12] Gludovatz B, Hohenwarter A, Catoor D, Chang EH, George EP, Ritchie RO. A fracture-resistant high-entropy alloy for cryogenic applications. Science 2014;345:1153–8.

[13] Guo X, Xie X, Ren J, Laktionova M, Tabachnikova E, Yu L, Cheung W-S, Dahmen KA, Liaw PK. Plastic dynamics of the Al0.5CoCrCuFeNi high entropy alloy at cryogenic temperatures: Jerky flow, stair-like fluctuation, scaling behavior, and non-chaotic state. Applied Physics Letters 2017;111:251905.

[14] Hähner P, Zaiser M. From mesoscopic heterogeneity of slip to macroscopic fluctuations of stress and strain. Acta Materialia 1997;45:1067–75.

[15] Kim J-H, Kim S-K, Lee C-S, Kim M-H, Lee J-M. A constitutive equation for predicting the material nonlinear behavior of AISI 316L, 321, and 347 stainless steel under low-temperature conditions. International Journal of Mechanical Sciences 2014;87:218–25.

[16] Klose FB, Ziegenbein A, Weidenmüller J, Neuhäuser H, Hähner P. Portevin–LeChatelier effect in strain and stress controlled tensile tests. Computational Materials Science 2003;26:80–6.

[17] Koch CC, Easton DS. A review of mechanical behaviour and stress effects in hard superconductors. Cryogenics 1977;17:391–413.

[18] Kocks UF, Mecking H. Physics and phenomenology of strain hardening: the FCC case. Progress in Materials Science 2003;48:171–273.

[19] Kubin LP, Chihab K, Estrin Y. The rate dependence of the portevin-Le chatelier effect. Acta Metallurgica 1988;36:2707–18.

[20] Lebyodkin MA, Dunin-Barkovskii LR, Bobrov VS, Gröger V. Statistical aspects of low temperature discontinuous deformation. Scripta Metallurgica et Materialia 1995;33:773–80.

[21] Ma A, Roters F, Raabe D. A dislocation density based constitutive model for crystal plasticity FEM including geometrically necessary dislocations. Acta Materialia 2006;54:2169–79.

[22] Mansouri LZ, Thuillier S, Manach PY. Thermo-mechanical modeling of Portevin–Le Châtelier instabilities under various loading paths. International Journal of Mechanical Sciences 2016;115-116:676–88.

[23] Mecking H, Kocks UF. Kinetics of flow and strain-hardening. Acta Metallurgica 1981;29:1865–75.

[24] Nalepka, K., Skoczeń, B., Ciepielowska, M., Schmidt, R., Tabin, J., Schmidt, E., Zwolińska-Faryj, W., R., C., 2021. Phase transformation in 316L austenitic steel induced by fracture at cryogenic temperatures: experiment and modelling. (under review).

[25] Obst B, Nyilas A. Experimental evidence on the dislocation mechanism of serrated yielding in f.c.c. metals and alloys at low temperatures. Materials Science and Engineering: A 1991;137:141–50.

[26] Obst B, Nyilas A. Time-resolved flow stress behavior of structural materials at low temperatures. In: Advances in Cryogenic Engineering, 44. New York: Plenum Press; 1998. p. 331–8.

[27] Ogata T, Ishikawa K. Time-dependent deformation of austenitic stainless steels at cryogenic temperatures. Cryogenics 1986;26:365–9.

[28] Olson GB, Cohen M. A mechanism for the strain-induced nucleation of martensitic transformations. Journal of the Less Common Metals 1972;28:107–18.

[29] Portevin A, Le Chatelier F. Sur un phénomène observé lors de l'essai de traction d'alliages en cours de transformation. Comptes Rendus de l'Académie des Sciences Paris 1923;176:507–10.

[30] Pu Z, Xie ZC, Sarmah R, Chen Y, Lu C, Ananthakrishna G, Dai LH. Spatio-temporal dynamics of jerky flow in high-entropy alloy at extremely low temperature. Philosophical Magazine 2021;101:154–78.

[31] Pustovalov VV. Serrated deformation of metals and alloys at low temperatures (Review). Low Temperature Physics 2008;34:683–723.

[32] Reed RP, Mikesell RP, Clark AF. Low Temperature Tensile Behavior of Copper-Stabilized Niobium-Titanium Superconducting Wire. In: Advances in Cryogenic Engineering, 22. Boston, MA: Springer US; 1977. p. 463–71.

[33] Reed RP, Simon NJ. Discontinuous yielding in austenitic steels at low temperatures. International Cryogenic Material Boulder 1988:851–63.

[34] Reed RP, Walsh RP. Tensile strain rate effect in liquid helium. Adv. Cryogenic Engineering Materials 1988;34:199–208.

[35] Rezaee-Hajidehi M, Stupkiewicz S. Modelling of propagating instabilities in pseudoelastic NiTi tubes under combined tension–torsion: helical bands and apparent yield locus. International Journal of Solids and Structures 2020.

[36] Rizzi E, Hähner P. On the Portevin–Le Chatelier effect: theoretical modeling and numerical results. International Journal of Plasticity 2004;20:121–65.

[37] Schwarz RB, Mitchell JW. Dynamic dislocation phenomena in single crystals of Cu-10.5-at.%-Al alloys at 4.2 K. Phys. Rev 1974;B 9:3292–9.

[38] Seeger A. Dislocations and mechanical properties of crystals. New York: Wiley; 1957.

[39] Skoczeń B. Constitutive model of plastic strain induced phenomena at cryogenic temperatures. Journal of Theoretical and Applied Mechanics 2008;46:949–71.

[40] Skoczeń B, Bielski J, Sgobba S, Marcinek D. Constitutive model of discontinuous plastic flow at cryogenic temperatures. International Journal of Plasticity 2010;26:1659–79.

[41] Skoczeń B, Bielski J, Tabin J. Multiaxial constitutive model of discontinuous plastic flow at cryogenic temperatures. International Journal of Plasticity 2014;55:198–218.

[42] Spencer K, Véron M, Yu-Zhang K, Embury JD. The strain induced martensite transformation in austenitic stainless steels: Part 1 – Influence of temperature and strain history. Materials Science and Technology 2009;25:7–17.

[43] Tabachnikova ED, Dolgin AM, Bengus VZ, Yefimov YV. Fiz. Metallov Metallovedenie 1984:58.

[44] Tabin J, Prącik M. Methods for identifying dynamic parameters of clip-on extensometer–specimen structure in tensile tests. Measurement 2015;63:176–86.

[45] Tabin J, Skoczen B, Bielski J. Strain localization during discontinuous plastic flow at extremely low temperatures. International Journal of Solids and Structures 2016;97–98:593–612.

[46] Tabin J, Skoczen B, Bielski J. Damage affected discontinuous plastic flow (DPF). Mechanics of Materials 2017;110:44–58.

[47] Tabin J, Skoczen B, Bielski J. Discontinuous plastic flow coupled with strain induced fcc–bcc phase transformation at extremely low temperatures. Mechanics of Materials 2019;129:23–40.

[48] Tabin J, Skoczen B, Bielski J. Discontinuous plastic flow in superconducting multifilament composites. International Journal of Solids and Structures 2020;202:12–27.

[49] Tsai M-H, Yeh J-W. High-Entropy Alloys: A Critical Review. Materials Research Letters 2014;2:107–23.

[50] Vorob'ev EV. New types of limit states of structural alloys related to the realization of the low temperature discontinuous yielding effect. Mechanics 2006;57:17–21.

[51] Vorob'ev EV, Anpilogova TV. Kinetics of low-temperature discontinuous deformation of metals. Cryogenics 2015;68.

[52] Vorob'ev EV. Peculiarities of neck formation under low-temperature discontinuous yield of metals. Part 2. Plane strain. Strength of Materials 2008;40:439–44.

[53] Vorob'ev EV, Anpilogova TV. Numerical analysis of the deformation instability of metals in liquid helium. Computational Materials Science 2013;68:66–72.

[54] Wessel ET. Metals at Low Temperatures. Trans. ASM 1957;49:149.

[55] Wu H. An empirical non-proportional cyclic plasticity approach under multiaxial low-cycle fatigue loading. International Journal of Mechanical Sciences 2018;142-143:66–73.

[56] Zaiser M, Hähner P. Oscillatory Modes of Plastic Deformation: Theoretical Concepts. physica status solidi (b) 1997;199:267–330.

[57] Zhang P, Li J, Guo Q, Zhu Y, Yan K, Wang R, Zhang K, Liu X, Feng Y. Chapter 15 - NbTi superconducting wires and applications. In: Titanium for Consumer Applications. Elsevier; 2019. p. 279–96.

[58] Zhou T, Yu C, Kang G, Kan Q. A new microplane model for non-proportionally multiaxial deformation of shape memory alloys addressing both the martensite transformation and reorientation. International Journal of Mechanical Sciences 2019;152:63–80.

[59] Zinov'ev MV, Il'ichev VY, Rykov VA, Savva SP. Method of testing samples in a biaxial stressed state at low temperatures. Strength of Materials 1972;4:637–9.